



## RESEARCH ARTICLE

10.1029/2021MS002816

## Key Points:

- A Lagrangian plume model is created and embedded into a global Eulerian model to establish a Plume-in-Grid (PiG) model
- The PiG and global Eulerian models are compared by a 1-month simulation of continuous stratospheric emissions from an aircraft
- The PiG model resolves nonlinear plume-scale processes at a fraction of the computational cost of fine-resolution global Eulerian models

## Supporting Information:

Supporting Information may be found in the online version of this article.

## Correspondence to:

H. Sun,  
[hongwei\\_sun@g.harvard.edu](mailto:hongwei_sun@g.harvard.edu)

## Citation:

Sun, H., Eastham, S., & Keith, D. (2022). Developing a Plume-in-Grid model for plume evolution in the stratosphere. *Journal of Advances in Modeling Earth Systems*, 14, e2021MS002816. <https://doi.org/10.1029/2021MS002816>

Received 12 OCT 2021

Accepted 17 MAR 2022

## Author Contributions:

**Conceptualization:** Hongwei Sun, Sebastian Eastham, David Keith  
**Data curation:** Hongwei Sun  
**Formal analysis:** Hongwei Sun  
**Funding acquisition:** David Keith  
**Investigation:** Hongwei Sun  
**Methodology:** Hongwei Sun, Sebastian Eastham, David Keith  
**Project Administration:** David Keith  
**Resources:** Hongwei Sun, Sebastian Eastham, David Keith  
**Software:** Hongwei Sun, Sebastian Eastham, David Keith

© 2022 The Authors. Journal of Advances in Modeling Earth Systems published by Wiley Periodicals LLC on behalf of American Geophysical Union. This is an open access article under the terms of the [Creative Commons Attribution License](#), which permits use, distribution and reproduction in any medium, provided the original work is properly cited.

# Developing a Plume-in-Grid Model for Plume Evolution in the Stratosphere

Hongwei Sun<sup>1</sup> , Sebastian Eastham<sup>2,3</sup> , and David Keith<sup>1</sup> 

<sup>1</sup>Harvard John A. Paulson School of Engineering and Applied Sciences, Harvard University, Cambridge, MA, USA,

<sup>2</sup>Laboratory for Aviation and the Environment, Department of Aeronautics and Astronautics, Massachusetts Institute of Technology, Cambridge, MA, USA, <sup>3</sup>Joint Program on the Science and Policy of Global Change, Massachusetts Institute of Technology, Cambridge, MA, USA

**Abstract** Stratospheric emissions from aircraft or rockets are important sources of chemical perturbations. Small-radius high-aspect-ratio plumes from stratospheric emissions are smaller than global Eulerian models' grid cells. To help global Eulerian models resolve subgrid plumes in the stratosphere, a Lagrangian plume model, comprising a Lagrangian trajectory model and an adaptive-grid plume model with a sequence of plume cross-section representations (from a highly resolved 2-D grid to a simplified 1-D grid based on a tradeoff between the accuracy and computational cost), is created and embedded into a global Eulerian (i.e., GEOS-Chem) model to establish a multiscale Plume-in-Grid (PiG) model. We compare this PiG model to the GEOS-Chem model based on a 1-month simulation of continuous inert tracer emissions by aircraft in the stratosphere. In the PiG results, the final injected tracer is more concentrated and approximately 1/3 of the tracer is at concentrations 2–4 orders of magnitude larger compared to the GEOS-Chem results. The entropy of injected tracer in the PiG results is 6% lower than the GEOS-Chem results, indicating less tracer mixing. The total product mass from a hypothetical second-order process (applied to the injected tracer) in the PiG results is 2 orders of magnitude larger than the GEOS-Chem results. Increasing the GEOS-Chem model's horizontal resolution 4-fold is insufficient to resolve this product difference, while requiring over seven times the computational resources of the PiG model. This paper describes the PiG model framework and parameterization of plume physical processes. Chemical and aerosol processes will be introduced in the future.

**Plain Language Summary** Computer models used to understand how aircraft damage the environment usually split the atmosphere into large boxes with a length scale of ~100 km, ignoring smaller scale variations in pollutants inside the box. Pollution produced by aircraft is released in narrow plumes that are much smaller than the box. Some chemical or physical processes could occur much faster inside a high-concentration exhaust plume than when the same amount of pollution is spread out over the large box, which may produce big errors in calculating the impact of aircraft emissions in the stratosphere where plumes mix slowly. This also causes problems for predicting the impacts of solar geoengineering in which aircraft emit reflective material to cool the planet. One can fix the problem by making the boxes much smaller, which requires too much computer time to be practical. We describe a method using smaller boxes just where they are most needed at the plume. After the plume has spread a bit, our “plume-in-grid” model then eliminates the small boxes and gives the information back to the conventional computer model's big box. This can allow more accurate calculations of the impacts of pollution plumes for a given amount of computing time.

## 1. Introduction

Stratospheric emissions from aircraft or rockets can be an important source of chemical perturbations (Jacobson et al., 2013). Stratospheric solar geoengineering, for example, would almost certainly use aircraft for deployment, and these aircraft would produce high aspect-ratio plumes with strong concentration gradients. Commercial aircraft operating in the stratosphere will produce similar plumes. Global Eulerian models are widely employed to simulate the global climatic impact of long-term stratospheric emissions. However, plumes from aircraft and rockets can reach thousands of kilometers in length but just several kilometers in cross-sectional radius in the stratosphere. Observations have revealed that plumes diffuse slowly in the stratosphere and may maintain the small-radius high-aspect-ratio structure from days to weeks (Newman et al., 2001). Global Eulerian models cannot provide an overall adequate resolution everywhere to resolve plumes in the stratosphere. In a global Eulerian model, a given plume is instantly diluted into a large Eulerian grid cell, which results in an artificially

**Supervision:** Sebastian Eastham, David Keith

**Validation:** Hongwei Sun

**Visualization:** Hongwei Sun

**Writing – original draft:** Hongwei Sun

**Writing – review & editing:** Sebastian Eastham, David Keith

low and uniform plume concentration. Numerical diffusion in the global Eulerian model also introduces extra dispersion and reduces plume preservation (Eastham & Jacob, 2017; Zhuang et al., 2018), which underestimates plume concentration. The artificially lower plume concentration in the global Eulerian model produces errors in simulating nonlinear processes (Cameron et al., 2013; Meijer et al., 1997), introducing bias in the chemical reaction efficiency, particle size distribution, etc. For example, Cameron et al. (2013) modeled photochemistry based on aircraft emissions in an expanding plume versus at the grid scale in an atmospheric model. They found that the plume treatment decreased grid-scale ozone production by 33% at cruise altitude after a 10-hr simulation compared with the grid-scale treatment.

Various methods (Burkhardt & Kärcher, 2009; Georgopoulos & Seinfeld, 1986; Paoli, 2020; Paoli et al., 2011, 2020) have been developed to better simulate subgrid plumes in the stratosphere. Cariolle et al. (2009) used an effective reaction rate (ERR) method to parameterize the plume-scale chemistry into large-scale atmospheric models. McKenna et al. (2002) developed a Chemical Lagrangian Model of the Stratosphere (CLaMS), which could resolve small-scale elongated filaments in the stratosphere. Schumann (2012) applied a Lagrangian Gaussian plume model to simulate the advection and evolution of contrails formed along aircraft tracks. Pierce et al. (2010) adopted a well-mixed expanding Lagrangian-box version of the TwO-Moment Aerosol Sectional (TOMAS) microphysics model (Adams & Seinfeld, 2002) to model aerosol formation and growth within an aircraft plume in solar geoengineering. Most previous plume models assume either a Gaussian or a uniform distribution for the plume cross-section. In this study, we develop a new Lagrangian plume model, which adopts a more accurate representation of the plume cross-section (Section 2.3). We embed the Lagrangian plume model into a global Eulerian model to establish a multiscale Plume-in-Grid (PiG) model. Instead of instantly diluting the subgrid plume into a large Eulerian grid cell, the embedded Lagrangian plume model helps the global Eulerian model resolve and simulate small-radius high-aspect-ratio plumes in the stratosphere. When the plume grows sufficiently large and can be resolved by the host Eulerian model grid, the PiG model dissolves the plume from the Lagrangian plume model into the host Eulerian model.

One primary motivation for PiG model development is to simulate stratospheric aerosol injection (SAI) in solar geoengineering. By injecting aerosols into the stratosphere to reduce incoming shortwave radiation, solar geoengineering may mitigate some of the damage caused by global warming. One possible way to inject aerosols into the stratosphere is by employing aircraft. However, most studies directly apply the global Eulerian model to simulate long-term aircraft emissions for SAI purposes, which cannot adequately resolve aircraft plumes. Previous studies (Dai et al., 2018; Golja et al., 2021; Pierce et al., 2010; Tilmes et al., 2018; Vattioni et al., 2019) have found that the climatic impacts of SAI are sensitive to the injection strategy (e.g., pulse or point emissions), injected sulfur form (e.g., accumulation-mode  $\text{H}_2\text{SO}_4$  droplets or gas-phase  $\text{SO}_2$ ), injection location (latitude, altitude), injection time (summer, winter), etc. However, no studies have evaluated the influence of two different model types (Eulerian model vs. Lagrangian model) on simulating SAI's climatic impacts. In this study, we compare the plume dispersion of an inert tracer from 1-month SAI aircraft emissions between two types of models, namely, the global Eulerian model, which instantly dilutes subgrid plumes into large Eulerian grid cells, and the PiG model, which resolves and simulates subgrid plumes with the embedded plume model.

Section 2 describes the Lagrangian plume model parameterization and the new PiG model development. Section 3 evaluates the parameterization applied to resolve the plume cross-section in the plume model. Section 4 compares the PiG model to a standard global Eulerian (GEOS-Chem) model regarding plume evolution in the stratosphere. Finally, Section 5 presents the conclusions and discussions.

## 2. Model Description

The multiscale PiG model incorporates a Lagrangian plume model into a global Eulerian model (Figure 1). This study uses GEOS-Chem version 13.0.0 (<https://doi.org/10.5281/zenodo.4618180>) as the global Eulerian model (Section 4.1), but the approach described in this section is general enough to be applied to other global Eulerian models. The Lagrangian plume model comprises a Lagrangian trajectory model and an adaptive-grid plume model, which can resolve subgrid plumes in the stratosphere. While more fine-grained approaches such as large eddy simulation might provide a more accurate representation of an individual plume, our PiG model bridges the gap between the scales of the global Eulerian grid and subgrid plumes. Physical processes, such as advection and diffusion, are simulated in the Lagrangian plume model based on meteorological data acquired from the

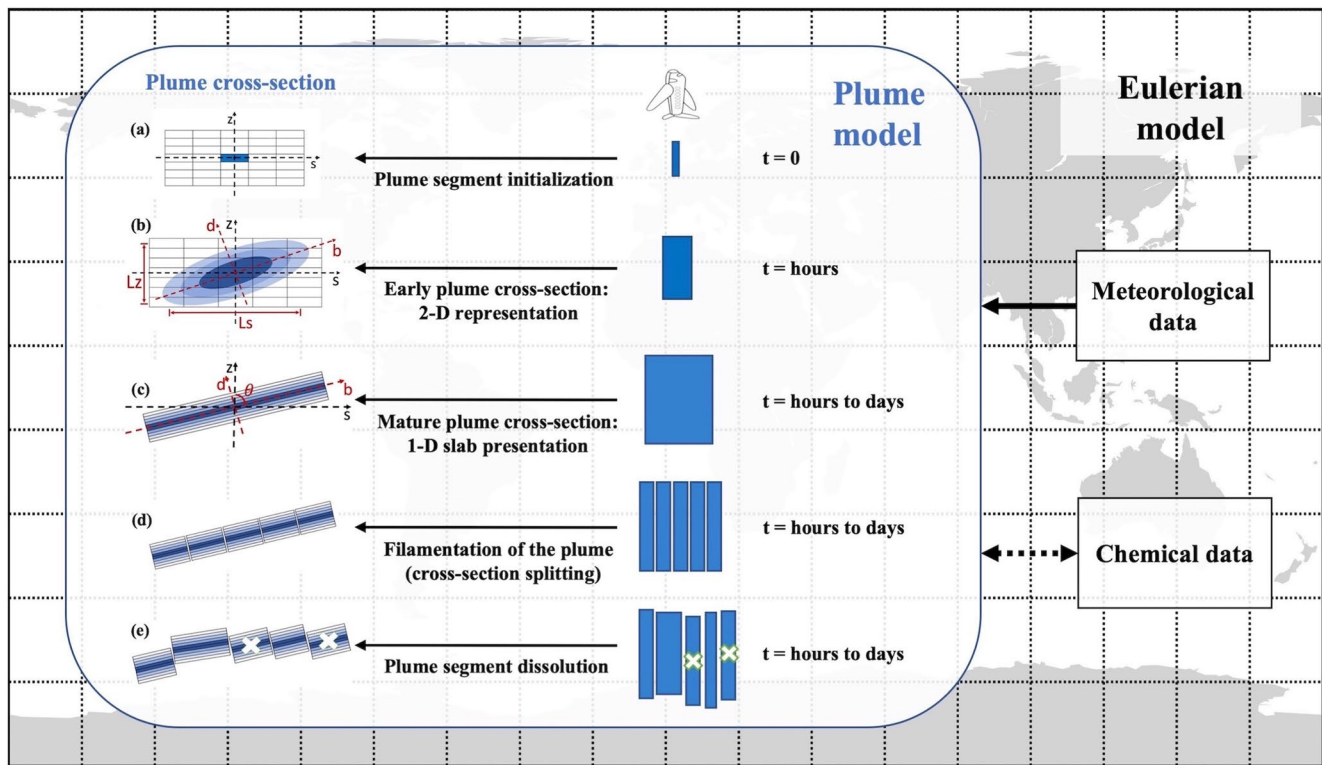


**Figure 1.** Schematic framework of the Plume-in-Grid (PiG) model (a global Eulerian model with an embedded Lagrangian plume model). The interaction of chemical data between the plume model and the host Eulerian model will be fully implemented in the PiG model in the future (though not in this study) when aerosol and chemical processes are considered.  $t$  represents the lifetime of the plume segment. The plume segment is initially injected at  $t = 0$ .  $L_s$  and  $L_z$  denote the horizontal and vertical length scales of the plume cross-section, respectively (defined in Section 2.3.1). Axes  $\bar{s}$  and  $\bar{z}$  represent the horizontal and vertical directions, respectively. Axes  $\bar{b}$  and  $\bar{d}$  are along the directions of the breadth (B) and depth (D) of the 1-D grid (Section 2.3.2) cell, respectively.  $\theta$  is the tilting angle of the plume segment cross-section between the cross-sectional breadth and vertical direction.

host Eulerian model. The injected tracer in the plume model can be released into the host Eulerian model if the tracer is transported outside of the plume model grid domain due to diffusion, wind shear, etc. Once the plume grows sufficiently large to be resolved by the host Eulerian model grid, the PiG model removes the plume from the Lagrangian plume model and incorporates it into the host Eulerian model. Thus, the embedded Lagrangian plume model acts as a subgrid model to help the host Eulerian model overcome its inability to resolve subgrid plumes in the stratosphere. In this study, we focus on the physical evolution of plumes in the stratosphere without considering aerosol and chemical processes, the injected tracer concentrations in the plume (simulated by the plume model) are treated as perturbations to the host Eulerian grid concentrations on which the plume is overlaid (Karamchandani et al., 2000, 2006).

## 2.1. Plume Segment Initialization

The emissions from aircraft or rockets make small-radius high-aspect-ratio plumes in the stratosphere. The Lagrangian plume model divides the initially injected plume into segments and describes each plume segment by the plume segment center location, plume segment length ( $L$ ), and plume segment cross-section. The initial plume segment length is set as  $1/N_s$  ( $N_s$  is a defined integer, which is 5 in this study) of the horizontal grid size of the host Eulerian model. Because the horizontal grid size of the host Eulerian model is approximately 200 km in this study, the initial plume segment length is set to approximately 40 km, which is  $1/5$  ( $N_s = 5$ ) of the horizontal grid size.  $N_s$  is also treated as the splitting number in Section 2.4. For example, when the plume segment length grows larger than the horizontal grid size of the host Eulerian model, the plume segment (with a length of  $L$ ) is evenly split into  $N_s$  smaller plume segments (with a length of  $L/N_s$ ). These approaches (here and in Section 2.4) ensure that plume segments are always smaller than the grid spacing of the host Eulerian model, reducing the possibility that a single plume segment covers heterogeneous background conditions. In the plume segment, the

concentration along the flight direction (along the plume segment length) is assumed to be uniform, while the cross-sectional concentration distribution is captured by an adaptive grid in the plume model (Section 2.3).

## 2.2. Plume Segment Movement, Expansion, and Horizontal Stretching

### 2.2.1. Movement

A Lagrangian trajectory model is created and incorporated into the plume model to track the location of each plume segment center based on  $d\vec{s} = \vec{u} \cdot dt$ , where  $d\vec{s}$  is the movement distance of the plume segment,  $dt$  is the plume model time step, and  $\vec{u}$  is the wind speed interpolated (using inverse distance weighting interpolation) from the meteorological data provided by the host Eulerian model. The 4th-order Runge Kutta method is adopted to calculate the movement distance. To avoid the Pole singularity problem in the regular latitude-longitude mesh, a polar stereographic plane (Dong & Wang, 2012) is applied in the polar region (where the latitude exceeds 72°) to calculate the plume segment movement in the plume model.

### 2.2.2. Expansion

The plume model calculates the plume segment volume ( $V$ ) change when the background pressure ( $P$ ) and temperature ( $T$ ) vary during plume segment movement in the stratosphere, according to the ideal gas law. The plume segment volume change is reflected by the change of grid cell size in the Lagrangian plume model. The pressure and temperature considered in the plume model are provided by the host Eulerian model (Figure 1).

### 2.2.3. Horizontal Stretching

Since the wind field in the stratosphere is not uniform, the horizontal wind shear can stretch the plume segment along its length. According to previous studies (Eastham & Jacob, 2017; Rastigejev et al., 2010), the horizontal stretching of the plume segments is calculated based on the Lyapunov exponent ( $\lambda$ ) of flow:

$$L(t + \Delta t) = e^{\lambda \Delta t} L(t) \quad (1)$$

where  $L$  is the plume segment length and  $t$  is the plume segment lifetime (the plume segment is initially injected at  $t = 0$ ). The Lyapunov exponent is calculated based on  $\lambda = \frac{\Delta u}{\Delta x}$ , where  $\Delta u$  and  $\Delta x$  are the wind speed and distance changes between the current grid cell (including the plume segment) and the downstream grid cell in the host Eulerian grid, respectively. To conserve the plume segment volume ( $V$ ) during the stretching process, the plume segment cross-sectional area ( $A$ ) should decrease/increase corresponding to the plume segment length ( $L$ ) expansion/contraction, that is,  $A(t + \Delta t)L(t + \Delta t) = A(t)L(t) = V$ . The Lagrangian plume model changes its grid cell size to reflect the change of the plume segment cross-section ( $A$ ) and length ( $L$ ). Plume segment length can become very large (i.e., commensurate with the horizontal grid size of the host Eulerian model) because of horizontal stretching, which results in plume splitting along the plume segment length (Section 2.4).

## 2.3. Representation of the Plume Segment Cross-Section Over Time

The Lagrangian plume model in this study focuses on simulating plume evolution in the diffusion regime (Fritz et al., 2020; Kärcher, 1995) when plume cross-section evolution is mainly influenced by diffusion and vertical wind shear in the stratosphere (Dürbeck & Gerz, 1995; Naiman et al., 2010; Schumann et al., 1995). Vertical wind shear ( $S$ ) can alter the cross-sectional concentration distribution through plume segment cross-sectional distortion. In the plume model, the vertical wind shear is calculated as  $S = du_s/dz$ , where  $u_s$  is the horizontal wind speed along the plume segment cross-section, and  $z$  is the vertical height. Vertical and horizontal diffusion can dilute the plume segment cross-sectional concentration. The vertical diffusion coefficient is calculated based on  $D_v = \frac{C_v}{N_{BV}} w_N'^2$ , where  $C_v = 0.2$ , the vertical turbulence fluctuation ( $w_N'$ ) is set to 0.1 m s<sup>-1</sup>, and  $N_{BV}$  is the Brunt-Vaisala frequency (Schumann, 2012; Schumann et al., 1995). The horizontal diffusion coefficient is defined as a constant (10 m<sup>2</sup> s<sup>-1</sup>) (Dürbeck & Gerz, 1995, 1996; Schumann et al., 1995).

Various methods have been adopted to simulate the dilution process along the plume segment cross-section (Paoli et al., 2011). Naiman et al. (2010) applied an ellipse with three degrees of freedom (two radii and one rotational angle) to represent the plume segment cross-section and assumed a uniform cross-sectional concentration distribution. Kraabøl et al. (2000) employed eight circular or elliptical layers to resolve the concentration gradient along the plume cross-section. Focusing on the plume evolution in the stratosphere, we found that the

plume segment cross-section undergoes rapid horizontal diffusion at the early stage (the first several hours after injection). As soon as the plume segment cross-section has a high aspect ratio (cross-sectional horizontal scale to vertical scale), horizontal diffusion has negligible consequences for cross-sectional concentration dilution. This is verified in Section 2.3.1 and Supporting Information (Text S1 in Supporting Information S1). Thus, the adaptive grid in the plume model consists of a sequence of two high-resolution grids to resolve the plume segment cross-section, namely, a two-dimensional (2-D) representation of the early plume segment cross-section (Section 2.3.1) and a computationally efficient one-dimensional (1-D) representation of the mature plume segment cross-section (Section 2.3.2) when horizontal diffusion is negligible.

### 2.3.1. Early Plume Segment Cross-Section: 2-D Representation

As shown in Figures 1a and 1b, a 2-D high-resolution rectangular grid is adopted to simulate the plume segment cross-sectional concentration distribution at the early stage. Compared to the standard global Eulerian model resolution (a horizontal resolution of approximately  $10^4$ – $10^5$  m and a vertical resolution of  $\sim 10^3$  m), the cross-sectional 2-D grid in the plume model adopts a far-higher resolution (a horizontal resolution of  $\sim 10^2$  m and a vertical resolution of  $\sim 10$  m) to resolve the early cross-sectional concentration distribution of the plume segment.

*Diffusion.* The cross-sectional dilution caused by vertical and horizontal diffusion is calculated in the 2-D high-resolution grid as:

$$\frac{\partial C}{\partial t} = D_h \frac{\partial^2 C}{\partial s^2} + D_v \frac{\partial^2 C}{\partial z^2} \quad (2)$$

where  $C$  is the cross-sectional concentration,  $t$  is the time,  $D_h$  and  $D_v$  are the horizontal and vertical diffusion coefficients, respectively, and  $s$  and  $z$  (as shown in Figures 1a and 1b) are the horizontal and vertical distances, respectively, in the plume segment cross-section.

*Vertical wind shear.* The cross-sectional distortion attributed to the vertical wind shear is calculated as  $\partial C / \partial t = -u \partial C / \partial s$ , where  $u(s, z) = S \cdot z$  is a horizontal wind field defined based on the vertical wind shear ( $S$ ),  $C(s, z)$  is the cross-sectional concentration distribution, and  $(\vec{s}, \vec{z})$  is the Cartesian coordinate system in the cross-sectional 2-D grid domain (as shown in Figures 1a and 1b).

In the plume model, the cross-sectional 2-D grid resolution ( $ds \times dz$ ) changes in three situations ( $ds$  and  $dz$  always change proportionally):

1. When the plume segment volume increases/decreases because of pressure and temperature changes (ideal gas law), both the plume segment length ( $L$ ) and cross-sectional 2-D grid cell area ( $ds \times dz$ ) increase/decrease proportionally.
2. When the plume segment length expands/contracts due to horizontal wind shear, the cross-sectional 2-D grid cells decrease/increase to ensure plume segment volume conservation during the horizontal stretching process.
3. When the 2-D grid cell is too small to meet the Courant–Friedrichs–Lewy (CFL) condition for diffusion and advection processes, every  $3 \times 3$  grid cells in the cross-sectional 2-D grid are merged into 1 grid cell. The CFL condition for diffusion is  $\frac{\Delta t}{\Delta x^2} < \frac{1}{2D_k}$ ,  $\Delta t$  (unit: s) is the time step, and  $\Delta x$  (unit: m) and  $D_k$  (unit:  $\text{m}^2 \text{s}^{-1}$ ) are the grid cell spacing and diffusion coefficient along the direction of  $\vec{x}$ , respectively. The CFL condition for advection is  $\frac{u \Delta t}{\Delta x} < 1$ , where  $\Delta t$  is the time step, and  $\Delta x$  and  $u$  are the grid cell spacing and wind speed along the direction of  $\vec{x}$ , respectively. In our case,  $\vec{x}$  refers to  $\vec{s}$  or  $\vec{z}$  in the plume segment cross-section (Figures 1a and 1b).

As the plume segment develops, the influence of horizontal diffusion on the cross-sectional dilution continuously decreases and eventually becomes negligible compared to the influence of vertical diffusion. This can be verified through scale analysis. The scales of the vertical and horizontal diffusion terms in Equation 2 are  $|D_v| \frac{|C|}{|L_z|^2}$  and  $|D_h| \frac{|C|}{|L_s|^2}$ , respectively.  $L_z$  and  $L_s$  (in Figure 1b) denote the vertical and horizontal length scales, respectively, of the cross-section, which contains approximately 95% of the injected tracer mass:

$$\int_{-L_z/2}^{+L_z/2} \int_{-\infty}^{+\infty} C_{2D}(s, z) ds dz \approx 0.95 \int_{-\infty}^{+\infty} \int_{-\infty}^{+\infty} C_{2D}(s, z) ds dz \quad (3)$$



$$\int_{-L_s/2}^{+L_s/2} \int_{-\infty}^{+\infty} C_{2D}(s, z) dz ds \approx 0.95 \int_{-\infty}^{+\infty} \int_{-\infty}^{+\infty} C_{2D}(s, z) dz ds \quad (4)$$

where  $C_{2D}(s, z)$  is the cross-sectional concentration distribution based on the Cartesian coordinate system  $(\vec{s}, \vec{z})$  built in the 2-D grid (Figure 1b). The vertical wind shear can elongate the horizontal cross-sectional length scale  $L_s$  through cross-sectional distortion (Dürbeck & Gerz, 1996; Konopka, 1995), which in turn decreases  $|D_h| \frac{|C|}{|L_s|^2}$ . Thus, the vertical diffusion term can greatly exceed the horizontal diffusion term. Once the vertical diffusion term is 10 times as large as the horizontal diffusion term  $\left( \frac{D_v \frac{|C|}{|L_z|^2}}{D_h \frac{|C|}{|L_s|^2}} \geq 10 \right)$ , which requires the cross-sectional scale ratio to adhere to  $R_s = \frac{|L_s|}{|L_z|} \geq \sqrt{10 \frac{D_h}{D_v}}$ , the horizontal diffusion is considered negligible. As verified by the CONTROL (with horizontal diffusion) and SENSITIVITY (without horizontal diffusion once  $R_s \geq \sqrt{10 \frac{D_h}{D_v}}$ ) simulations in the Supporting Information (Text S1 in Supporting Information S1), the final cross-sectional concentration distribution is similar between the CONTROL and SENSITIVITY simulations (Figure S1 in Supporting Information S1), and the center concentration percentage difference between the two simulations is less than 1%.

In the stratosphere, the typical values for  $D_h$  and  $D_v$  are 10 and  $0.15 \text{ m}^2 \text{ s}^{-1}$ , respectively (Dürbeck & Gerz, 1995; Schumann et al., 1995). Therefore, once the plume cross-sectional scale ratio ( $R_s$ ) is higher than  $25 \left( \sqrt{10 \frac{D_h}{D_v}} \approx 25 \right)$  in the stratosphere, the early plume segment cross-section transitions into the mature plume segment cross-section. Horizontal diffusion becomes negligible along the mature plume segment cross-section, and only vertical diffusion and vertical wind shear play an essential part in the mature plume segment cross-section. A more straightforward but computationally efficient 1-D slab grid replaces the 2-D grid to resolve the mature plume segment cross-sectional concentration distribution, which can be considered as dimension reduction (Figures 1b and 1c).

### 2.3.2. Mature Plume Segment Cross-Section: 1-D Slab Presentation

After dimension reduction (from the 2-D to 1-D grid), the cross-sectional 1-D grid (Figure 1c) comprises long and thin slabs with three degrees of freedom, that is, the breadth ( $B$ ), depth ( $D$ ), and tilting angle ( $\theta$ ).  $\theta$  is the angle between the cross-sectional breadth and vertical direction, as shown in Figure 1c. The initial tilting angle ( $\theta$ ) of the 1-D slab grid is calculated based on the length scale ( $R_s$ ) of the cross-sectional 2-D grid:  $\theta = \arctan(R_s)$ . Since  $R_s$  is approximately 25 when we replace the cross-sectional 2-D grid with the cross-sectional 1-D grid, the initial tilting angle is approximately  $87.7^\circ$ . The initial depth ( $D$ ) of the 1-D slab grid is defined similarly to the vertical resolution ( $dz$ ) of the cross-sectional 2-D grid ( $D = dz$ ). The initial breadth ( $B$ ) of the 1-D slab grid adopts the value of the horizontal length scale ( $L_s$ ) of the cross-sectional 2-D grid ( $B = L_s$ ). The total number of 1-D grid cells ( $N_d$ ) is the same as the number of grid cells along the vertical direction of the cross-sectional 2-D grid.

The initial concentration distribution in the cross-sectional 1-D grid is calculated based on the concentration distribution in the cross-sectional 2-D grid. First, we use an interpolation method (bilinear and conservative interpolation methods are available in the source code) to map the 2-D concentration distribution  $C_{2D}(s, z)$  in the  $(\vec{s}, \vec{z})$  coordinate system onto the concentration distribution  $C_{P2d}(b, d)$  in the  $(\vec{b}, \vec{d})$  coordinate system (Figure 1b). Then the concentration distribution  $C_{P2d}(b, d)$  is integrated along the  $\vec{b}$  axis of the whole cross-section and divided by the initial breadth ( $B$ ) to obtain the initial 1-D concentration distribution in each 1-D grid cell  $C_{P1d}(d)$ , as shown in Figures 1b and 1c:

$$C_{P1d}(d) = \frac{1}{B} \int C_{P2d}(b, d) db \quad (5)$$

Because the 2-D grid (Figure 1b) cannot exactly overlap with the 1-D grid (Figure 1c), some of the injected tracer mass (located outside the 1-D grid domain) leaks during the interpolation from the 2-D grid to the 1-D grid (the 1-D grid is generally smaller than the 2-D grid). This leakage of the tracer mass, which is less than 1% of the total tracer mass in the initial 2-D grid, is added to the host Eulerian model to ensure that the total mass of the injected tracer is conserved. After the initial condition ( $B, D, \theta, C_{P1d}$ ) of the cross-section 1-D grid is attained in the plume model, the 1-D slab grid calculates the cross-sectional dilution under the influence of vertical diffusion and vertical wind shear, thereby ignoring horizontal diffusion.

*Vertical Diffusion.* The cross-sectional concentration ( $C$ ) dilution due to vertical diffusion is calculated as:

$$\frac{\partial C}{\partial t} = D_d \frac{\partial^2 C}{\partial d^2} \quad (6)$$

where  $D_d = D_v \sin(\theta)$  is the diffusion coefficient component along the direction of  $\vec{d}$ , and  $\vec{d}$  is the axis in the  $(\vec{b}, \vec{d})$  coordinate system, as shown in Figure 1c. Moreover,  $D_v$  is the vertical diffusion coefficient.

*Vertical wind shear.* According to Equations 5–7 of Naiman et al. (2010), the vertical wind shear ( $S$ ) can rotate and elongate the 1-D slab grid. Thus, the vertical wind shear influences the breadth ( $B$ ), depth ( $D$ ), and tilting angle ( $\theta$ ) as follows:

$$\frac{d\theta}{dt} = S \cos^2 \theta \quad (7)$$

$$\frac{dB}{dt} = B S \sin \theta \cos \theta \quad (8)$$

$$\frac{DD}{dt} = -D S \sin \theta \cos \theta \quad (9)$$

Similar to the cross-sectional 2-D grid, the 1-D slab grid resolution ( $B \times D$ ) can also change in three situations ( $B$  and  $D$  change proportionally):

1. When the plume segment volume increases/decreases because of pressure and temperature changes (ideal gas law), both the plume segment length ( $L$ ) and cross-sectional 1-D grid cell area ( $B \times D$ ) would increase/decrease proportionally.
2. When the plume segment length is elongated/contracted by horizontal wind shear, the cross-sectional 1-D grid cells decrease/increase to ensure volume conservation during the horizontal stretching process.
3. When the cross-sectional 1-D grid cell is too small to meet the CFL condition of the diffusion process, each pair of grid cells is merged into 1 grid cell.

## 2.4. Filamentation of the Plume

### 2.4.1. Plume Segment Length Splitting

As described in Section 2.2, horizontal wind shear can stretch the plume segment length, making the plume segment length beyond the horizontal grid cell size of the host Eulerian model. To reduce the possibility that a long plume segment covers heterogeneous background conditions, the plume model evenly splits the original plume segment (with a length of  $L$ ) into  $N_s$  ( $N_s$  is the splitting number) smaller segments (each with a length of  $L/N_s$ ) once the original plume segment length is commensurate with the horizontal grid cell size of the host Eulerian model. After splitting, each new smaller plume segment exhibits the same cross-section as that of the original plume segment but only  $1/N_s$  of the original plume segment length, which is similar to the initial plume segment length set in Section 2.1.

### 2.4.2. Plume Segment Cross-Section Splitting

Because of the vertical wind shear, the breadth of the plume segment cross-section can reach several hundred kilometers, which would exceed the horizontal size of its host Eulerian grid cell. As shown Figure 1d, the plume segment cross-sectional breadth ( $B$ ) is split into  $N_s$  identical smaller parts when  $B$  is commensurate with the horizontal grid cell size of the host Eulerian model. After splitting, each smaller plume segment part exhibits the same plume segment length as that of the original plume segment, but the cross-sectional breadth reaches only  $1/N_s$  of the original plume segment cross-sectional breadth.

## 2.5. Plume Segment Dissolution

In the PiG model, the plume segment is dissolved from the embedded plume model into the host Eulerian model once the plume segment meets any of the following four criteria: (a) nonlinearity criterion, (b) volume criterion,

(c) location criterion, and (d) time criterion. After plume segment dissolution, the tracer concentration in the host Eulerian model grid cell is updated as:

$$C'_{Eu} = C_{Eu} + \frac{V_{Pl} \sum_{i=1}^{N_d} C_{Pl}(i)}{V_{Eu}} \quad (10)$$

where  $C_{Eu}$  and  $C'_{Eu}$  are the tracer concentrations in the host Eulerian model grid cell before and after plume segment dissolution, respectively.  $V_{Eu}$  is the volume of the host Eulerian model grid cell,  $N_d$  is the number of plume model grid cells representing the plume segment,  $C_{Pl}(i)$  is the tracer concentration in plume grid cell  $i$  ( $i = 1, 2, \dots, N_d$ ), and all plume model grid cells have the same volume  $V_{Pl}$ .

### 2.5.1. Nonlinearity Criterion

Many previous studies have applied a size criterion (the plume segment size commensurate with the host Eulerian model grid size) to dissolve the plume segment from the plume model into the host Eulerian model (Karamchandani et al., 2002, 2006). However, there remains a high concentration gradient within the plume segment when the plume segment size reaches the host Eulerian model grid size. The size criterion for plume dissolution ignores the high concentration gradient within the plume segment, which may introduce bias in the plume nonlinear process simulation. In this study, we adopt a nonlinearity criterion (the product of a nonlinear process before plume dissolution becomes commensurate with the product after plume dissolution) to dissolve the plume segment from the plume model to the host Eulerian model, which enables better estimations of nonlinear processes.

As our primary motivation for PiG model development, SAI modeling requires accurate estimation of aerosol processes since these aerosol processes, such as coagulation, can highly influence the particle size distribution of the injected aerosols (e.g., sulfate aerosols). Since many chemical and aerosol processes (e.g., aerosol coagulation) are second-order processes, we apply a hypothetical second-order chemical process to the injected tracer in this study for the nonlinearity criterion. In the future, the hypothetical second-order process will be replaced by real indicators (e.g., ozone production in the stratosphere) once aerosol and chemical processes are considered in the plume model. To simulate the second-order process in the PiG model, we need to consider the interaction of the nonlinear (here, second-order) process between the background (host Eulerian model) and plume segment (embedded plume model) (Karamchandani et al., 2000; Korsakissok & Mallet, 2010). Based on Equations 2 and 3 in Korsakissok and Mallet (2010), the total product concentration ( $P$ , from both the plume model and the host Eulerian model) of the hypothetical second-order process, from where the plume segment is overlaid, is updated as follows:

$$\frac{d[P]}{dt} = k([C_{Pl}] + [C_{Eu}])^2 = k([C_{Pl}]^2 + 2[C_{Pl}][C_{Eu}] + [C_{Eu}]^2) \quad (11)$$

where  $[C_{Pl}]$  is the injected tracer concentration (unit: molecules  $\text{cm}^{-3}$ ) in the plume segment,  $[C_{Eu}]$  is the injected tracer concentration in the background, and  $k$  (unit:  $\text{cm}^3 \text{ molecules}^{-1} \text{ s}^{-1}$ ) is a proportionality constant of the second-order process.  $d[P]/dt$  is the total production rate in the space where the plume segment (plume model) overlaps with the background (host Eulerian model), so  $d[P]/dt$  is dependent on the injected tracer concentration from both the plume segment and background ( $[C_{Pl}] + [C_{Eu}]$ ).

The product concentration in the background ( $P_{Eu}$ ) is updated as:

$$\frac{d[P_{Eu}]}{dt} = k[C_{Eu}]^2 \quad (12)$$

The product concentration in the plume segment ( $P_{Pl}$ ) is updated as:

$$\frac{d[P_{Pl}]}{dt} = \frac{d[P]}{dt} - \frac{d[P_{Eu}]}{dt} = k([C_{Pl}]^2 + 2[C_{Pl}][C_{Eu}]) \quad (13)$$

Regarding the nonlinearity criterion, we calculate the mass of the new product from the hypothetical second-order process before ( $P_{\text{before}} = k \sum_{i=1}^{N_b} (C_{Pl}^2(i) + C_{Pl}(i)C_{Eu}) \Delta t V_{Pl}$ ) and after ( $P_{\text{after}} = k (C_{Eu}^2 - C_{Eu}^2) \Delta t V_{Eu}$ ) plume segment dissolution in a given time step ( $\Delta t$ ), according to Equations 10–13. If the percentage difference of the new product mass ( $|\frac{P_{\text{after}} - P_{\text{before}}}{P_{\text{before}}}|$ ) is smaller than a defined critical percentage (e.g., 10% is used in Section 4), the plume segment meets the nonlinearity criterion and begins to dissolve from the plume model into the host



Eulerian model. Text S2 in the Supporting Information S1 presents the sensitivity of the PiG model results to different critical percentage levels (5% vs. 10%) in the nonlinearity criterion.

### 2.5.2. Volume Criterion

For all the plume segments in the same host Eulerian grid cell, the volume criterion ensures that the total volume of all plume segments (plume model grid cells) never exceeds a defined critical percentage (e.g., 30% is used in Section 4) of their host Eulerian grid cell volume. Once the total volume of all plume segments exceeds the defined critical percentage of the host Eulerian grid cell volume, the PiG model dissolves the plume segments into the host Eulerian model, starting from the largest plume segment. This dissolution process is continued until the total volume of plume segments is smaller than the critical percentage of the host Eulerian grid cell volume. Text S2 in the Supporting Information S1 presents the sensitivity of the PiG model results to different critical percentage levels (30% vs. 50%) in the volume criterion.

### 2.5.3. Location Criterion

The Lagrangian plume model created in this study focuses on simulating plumes in the stratosphere. When the plume segment enters the tropopause, plume evolution becomes different because of different environments in the troposphere (e.g., convective eddies), which is no longer suitable to be simulated by our plume model. Thus, the PiG model in this study dissolves the plume segment from the plume model into the host Eulerian model upon the plume segment reaches the tropopause.

### 2.5.4. Time Criterion

A maximum lifetime (e.g., 28 days is used in Section 4) is defined for the plume segment to remain in the plume model. Once the plume segment remains in the plume model longer than the maximum lifetime, the PiG model dissolves the plume segment from the plume model into the host Eulerian model.

## 3. Evaluation of Plume Cross-Sectional Parameterization

### 3.1. Cross-Sectional 2-D Grid Evaluation

An analytical Gaussian solution for anisotropic diffusion of an inert tracer in linear shear flow (Dürbeck & Gerz, 1996; Konopka, 1995; Walcek, 2004) is adopted to validate the 2-D grid representation of the early plume cross-section (Section 2.3.1) in the plume model. We apply both the cross-sectional 2-D grid in the plume model and analytical solutions to simulate plume cross-sectional evolution downwind of a hypothetical point source of inert tracer emission in the stratosphere. The initial inert tracer injected from the point source is set to 1 kg. In the stratosphere, typical parameter values include a vertical wind shear of  $0.002 \text{ s}^{-1}$ , a horizontal diffusion coefficient of  $10 \text{ m}^2 \text{ s}^{-1}$ , and a vertical diffusion coefficient of  $0.15 \text{ m}^2 \text{ s}^{-1}$  (Dürbeck & Gerz, 1995; Schumann et al., 1995). The cross-sectional concentration distribution of analytical solutions 1,000 s after injection is set as the initial condition of the cross-sectional 2-D grid simulation.

Figure 2 shows the cross-sectional concentration distribution after 48-hr simulations with the 2-D grid model and the corresponding analytical solutions. The cross-sectional concentration distributions simulated with the 2-D grid model are similar to the results obtained with analytical solutions, and their spatial correlation coefficient reaches 1.00. Slight differences (Figure 2c) between the two simulated concentration distributions are acceptable considering the discretization of the 2-D grid model. Figure 3 shows the concentration percentage difference between the 2-D grid model simulation and corresponding analytical solutions at the center of the plume cross-section (the black dot in Figure 1c). The percentage difference in center concentration between the two simulations is less than 1%.

### 3.2. Cross-Sectional 1-D Grid Evaluation

After cross-sectional 2-D grid model validation, we compare the cross-sectional 1-D grid model results to the corresponding 2-D grid model results. Initially, 1 kg inert tracer is injected into the center grid cell of the cross-sectional 2-D grid under the typical stratospheric parameter settings defined in Section 3.1. As shown in Figure 4, the cross-sectional 2-D grid simulates the cross-sectional concentration dilution under the diffusion and wind shear influence at the beginning. When the plume cross-sectional aspect ratio ( $R_s$ ) is large enough ( $R_s > 25$ ,

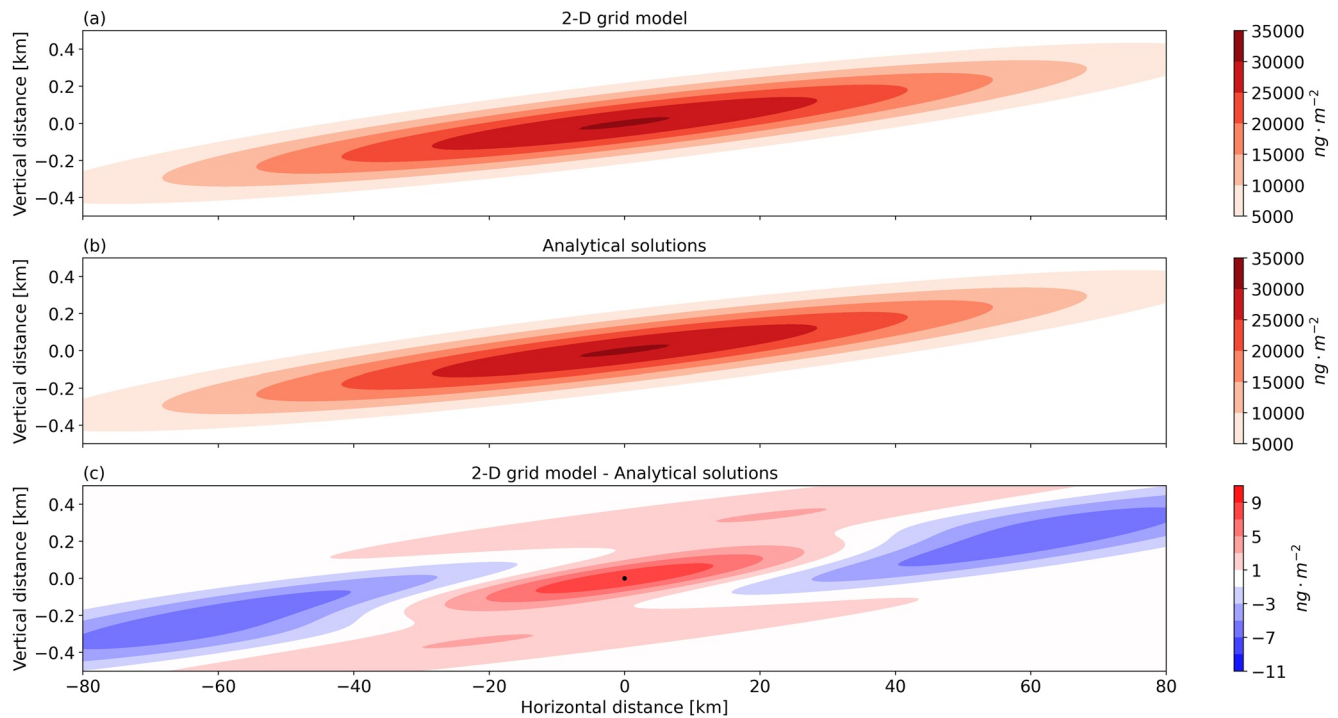


**Figure 2.** Plume cross-sectional concentration distribution from (a) the 48-hr simulation by the 2-D grid model, (b) corresponding analytical solutions, and (c) concentration difference between (a) and (b).

as described in Section 2.3.1), the concentration distribution in the cross-sectional 2-D grid is remapped onto the cross-sectional 1-D grid (Section 2.3.2). The 1-D grid replaces the 2-D grid to simulate the plume cross-sectional concentration distribution for 48 hr. The final 1-D grid model results are compared to the corresponding 2-D grid model results.

Figure 5 shows the final concentration distribution simulated with the 1-D grid model (blue solid line) and corresponding 2-D grid model (red dashed line). We find that the injected inert tracer dilutes faster in the cross-sectional 1-D grid, consistent with previous studies (e.g., Figure 7 in Naiman et al., 2010). The final center concentration in the cross-sectional 1-D grid model results is 9.4% lower than that in the cross-sectional 2-D grid model results (two black square points in Figure 5). Figure 6 shows that the percentage difference of the center concentration between the two models is smaller than 10%. The entropy (calculated based on Equation 14 in Section 4.2.2) of the concentration distribution is calculated to quantify how much extra tracer diffusion is caused by changing the 2-D grid to the 1-D grid. We found that the percentage difference of the final entropy between the 1-D and 2-D grid results is approximately 20%. However, for the same 48-hr simulation, the central processing unit (CPU) time required for the 1-D grid model is 20 s, while it is 30 min (1,800 s) for the 2-D grid model.

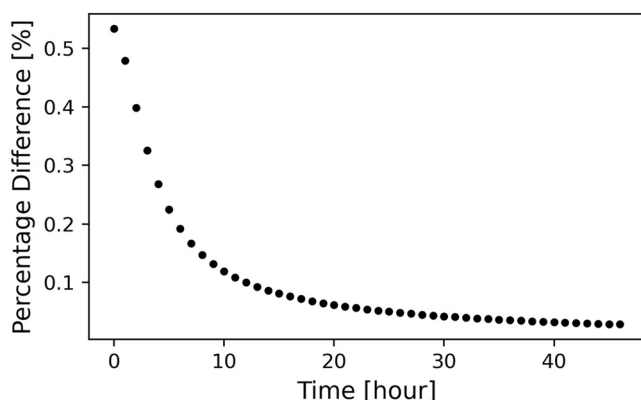


**Figure 3.** Concentration percentage difference between the 2-D grid model results and analytical solutions at the center of the plume cross-section (marked with a black dot in Figure 2c).

## 4. Global Modeling

### 4.1. Experiment Setting

We consider an inert tracer injection scenario using parameters that are relevant for the simulation of solar geoengineering to compare the PiG model with a conventional global Eulerian model (i.e., GEOS-Chem model in this study). This scenario assumes that an aircraft flies back and forth continuously at 240 m/s between 30°S and 30°N along a selected longitude line

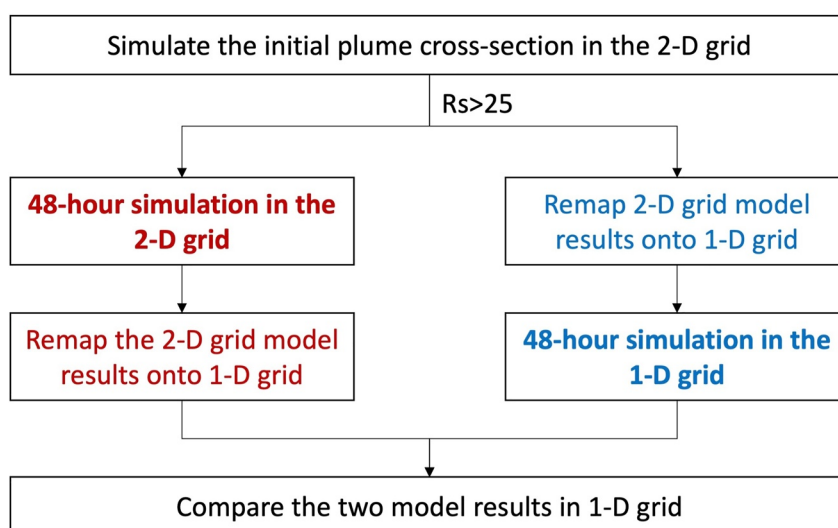


**Figure 4.** Schematic of the model result comparison between the 1-D and 2-D grid models.  $R_s$  is the cross-sectional scale ratio defined in Section 2.3.1.

(here,  $141^\circ\text{W}$ ) at a height of 50 hPa (approximately 20 km). An inert tracer is continuously injected by the aircraft at 30 kg/km along the flight track, a value chosen to be consistent with the fast dilution case in Pierce et al. (2010).

GEOS-Chem (Bey et al., 2001), a global three-dimensional (3-D) chemical transport model, is adopted as the host Eulerian model for the PiG model. The Lagrangian plume model created in this study is embedded into the GEOS-Chem model to build the PiG model. The horizontal resolution is  $2^\circ \times 2.5^\circ$  in the host GEOS-Chem model, which contains 72 vertical levels. Modern-Era Retrospective Analysis for Research and Applications-2 (MERRA2) data (Gelaro et al., 2017), with a horizontal resolution of  $0.5^\circ \times 0.625^\circ$ , provide the input meteorological data for the host GEOS-Chem model. The transport time step is 300 s in the GEOS-Chem model. Aerosol and chemical processes are turned off in the GEOS-Chem model as we only use inert tracer in this study.

The injected aircraft plume is divided into segments, and each plume segment is initially defined with a length of 40 km, which is approximately 1/5 of the horizontal grid size of the host GEOS-Chem model ( $2^\circ \times 2.5^\circ$ ). The initial cross-sectional 2-D grid resolution (Figure 1a) is set to 100 m ( $ds$ ) and 10 m ( $dz$ ). The initial domain size of the cross-sectional 2-D grid is approximately 20 km horizontally and 0.8 km vertically. As discussed in Section 2.3.1, the cross-sectional 1-D grid replaces the 2-D grid to represent the mature plume cross-section when

the plume cross-sectional scale ratio ( $R_s = L_y/L_z$ ) is higher than 25. Regarding plume filamentation (Section 2.4), the splitting number ( $N_s$ ) is set to 5 in this study. To achieve plume segment dissolution (Section 2.5), the critical percentage for the nonlinearity criterion is set to 10%. The critical percentage for the volume criterion is set to 30%. The maximum lifetime of the plume segment in the Lagrangian plume model is set to 4 weeks. Text S2 in the Supporting Information S1 describes the sensitivity of the PiG model results to different parameter settings under plume segment dissolution, including different settings for the nonlinearity and volume criteria. All the parameters defined here can be modified according to different research needs. For example, we can increase the resolution of the plume cross-sectional grid, which better resolves the plume cross-section but requires more computing resources. There is a trade-off between the model accuracy and computing efficiency when we adopt the PiG model to capture the plume-scale (i.e., subgrid) chemical and aerosol processes.

Both the PiG model and the standard GEOS-Chem model simulate aircraft plume evolution for 1 month (January 2015). The standard GEOS-Chem model uses the same settings as the host GEOS-Chem model in the PiG

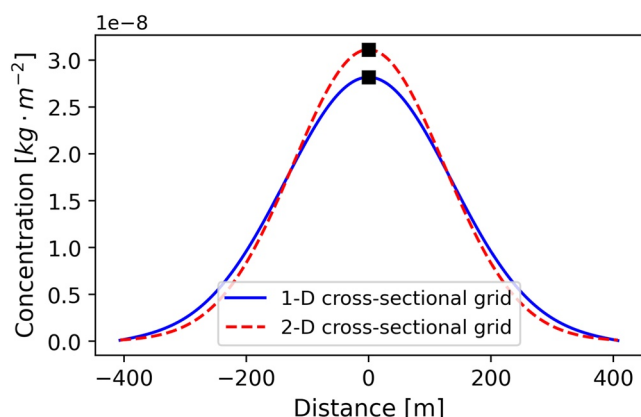


**Figure 5.** Final concentration distribution simulated in the cross-sectional 1-D (blue line) and 2-D (red dashed line) grid models. The x-axis is along the direction  $\vec{d}$  of the 1-D grid (Figure 1c).

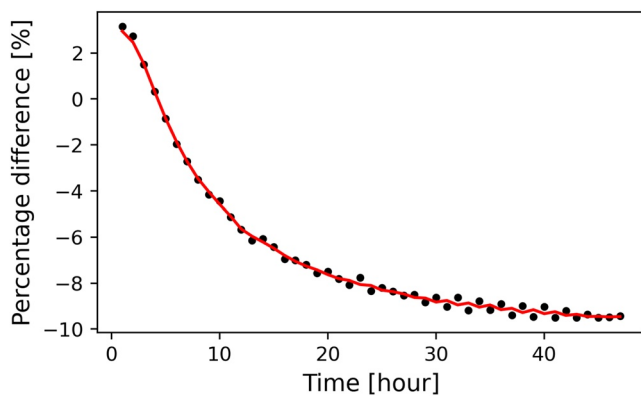


**Figure 6.** Final hourly mean concentration percentage difference (black dots) between the 1-D and 2-D grid model results (1-D minus 2-D) in the center grid cell (shown as the two black square points in Figure 5). The red line is the smoothing results after the 2-hr moving average.

model. In the standard GEOS-Chem model, the initially injected aircraft plume segment is instantly and uniformly dissolved into the Eulerian grid cell. In the PiG model, the initially injected aircraft plume segment is first simulated in the plume model and then dissolved into the host GEOS-Chem model. Figure 7a shows the number of plume segments of different types in the PiG model results. The active plume segments denote the plume segments simulated by the plume model. The dissolved plume segments indicate the plume segments already dissolved into the host GEOS-Chem model. The total plume segments encompass the sum of the active and dissolved plume segments. The increase in total plume segments is caused by the continuous injection and plume splitting (Section 2.4). Figure 7b shows the final plume segment lifetime distribution, which is the time that the plume segment remains in the plume model before its dissolution into the host GEOS-Chem model. The plume segment lifetime ranges from 0.2 to 28.0 days, with an average value of 8.5 days.

#### 4.2. Model Results Comparison

No single approach is appropriate for comparing the tracer distribution between the PiG and GEOS-Chem models because the differences in gridding are essential to assessing the performance of the PiG model. One approach, presented in Section 4.2.1, compares the two model results (PiG vs. GEOS-Chem) in the same Eulerian grid used by the GEOS-Chem model. In this method, the active plume segments from the final PiG model results are diluted into the host Eulerian grid. This method is appropriate for comparing the effect of the PiG model on the large-scale tracer distribution. However, this postprocessing approach can introduce extra plume dispersion and thus underestimate the tracer concentration in the PiG model results.

An alternative approach directly examines the tracer distribution over the active plume segments in the plume model grid as well as the host Eulerian grid. To implement this method, we must remove the volume of the active plume segment from the volume of the host Eulerian grid cell. Text S3 in the Supporting Information S1 describes this postprocessing approach in detail. The results of this method are presented in Section 4.2.2, where we also compute the entropy of the 3-D tracer mixing ratio field from the PiG and GEOS-Chem model results. The nonlinear process, which is highly dependent on the tracer concentration, is compared between the PiG and GEOS-Chem models in Section 4.2.3.

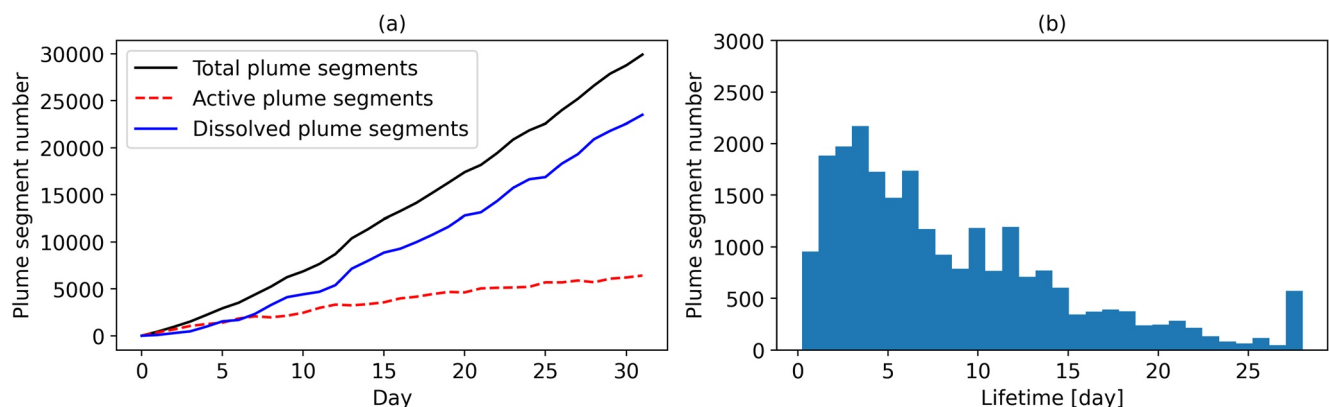


**Figure 7.** Description of the injected plume characteristics in the plume model. (a) The number of plume segments of different types. The active plume is the plume segment simulated by the plume model. The dissolved plume is the plume segment already dissolved into the host Eulerian model. The total plume segments encompass the sum of the active and dissolved plume segments. (b) The distribution of the plume segment lifetime (the time that the plume segment is simulated by the plume model).

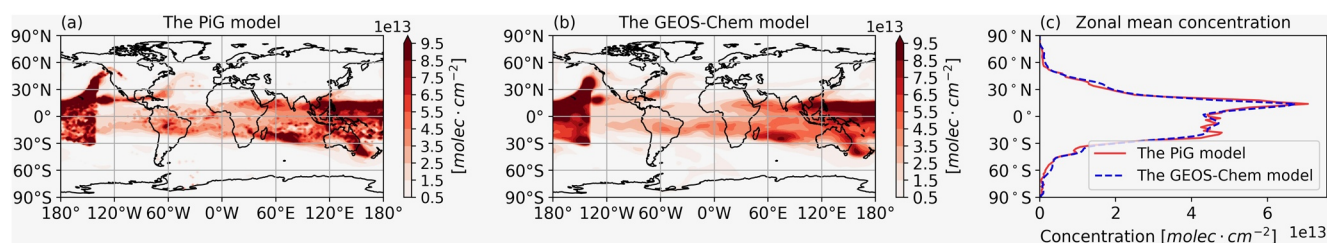


**Figure 8.** Final total column concentration of the injected tracer simulated by (a) the Plume-in-Grid (PiG) model, (b) the global Eulerian model, and (c) their zonal mean distributions.

#### 4.2.1. Horizontal and Vertical Concentration Distributions in the Eulerian Model Grid

**Horizontal concentration distribution.** Figures 8a and 8b show the total column concentration of the injected inert tracer simulated with the PiG and GEOS-Chem models at the end of the 1-month simulation. Since the PiG model can better preserve the plume segments, there are more high-concentration centers (high local concentration gradients) among the PiG model results (Figure 8a) than among the GEOS-Chem model results (Figure 8b). The standard deviation of the total column concentration from the PiG model is 11.79% larger than that from the GEOS-Chem model. For the zonal mean of the final total column concentration distribution, the GEOS-Chem model presents a smoother line than the PiG model (Figure 8c).

**Vertical concentration distribution.** Figures 9a and 9b show the zonal mean tracer concentrations at different heights after the 1-month simulation. There are  $3.9 \times 10^{31}$  molecules of the injected tracer within the initial injection area (60–40 hPa, 30°S to 30°N marked with dashed black boxes) in the PiG model, which is approximately 28% higher than the GEOS-Chem model results ( $3.0 \times 10^{31}$  molecules). Thus, the injected tracer is more concentrated in the initial injection area in the PiG model than in the GEOS-Chem model. Figure 9c shows the final vertical profile of the global mean tracer concentration. The global mean concentration at the injection height from the PiG model results is 29.5% larger than that from the GEOS-Chem model results (the two black dots in Figure 9c).

#### 4.2.2. Quantification of Tracer Diffusion

By using the postprocessing approach without plume dissolution (Text S3 in the Supporting Information S1), Figure 10a shows that, after a 1-month simulation, approximately 1/3 of the injected tracer remains in the active plume segments (plume model grid) in the PiG model, and is therefore at much higher tracer concentrations (2–4 orders of magnitude larger) than in the GEOS-Chem model. This is reasonable given that the Lagrangian plume model in the PiG model can resolve the plume segment and accurately represent the plume segment concentration. In the GEOS-Chem model, both the instant dilution of initially injected plume segments into the Eulerian grid and the numerical diffusion artificially decrease the plume tracer concentration.

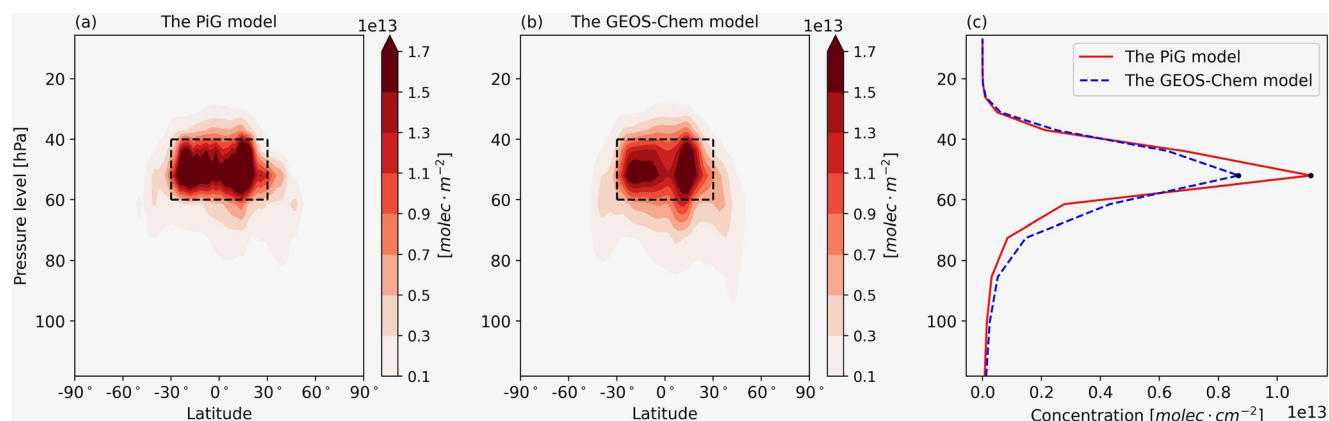


**Figure 9.** Final zonal mean concentration of the injected tracer from (a) the Plume-in-Grid (PiG) model and (b) the global Eulerian model and (c) corresponding global mean concentration at different pressure levels.



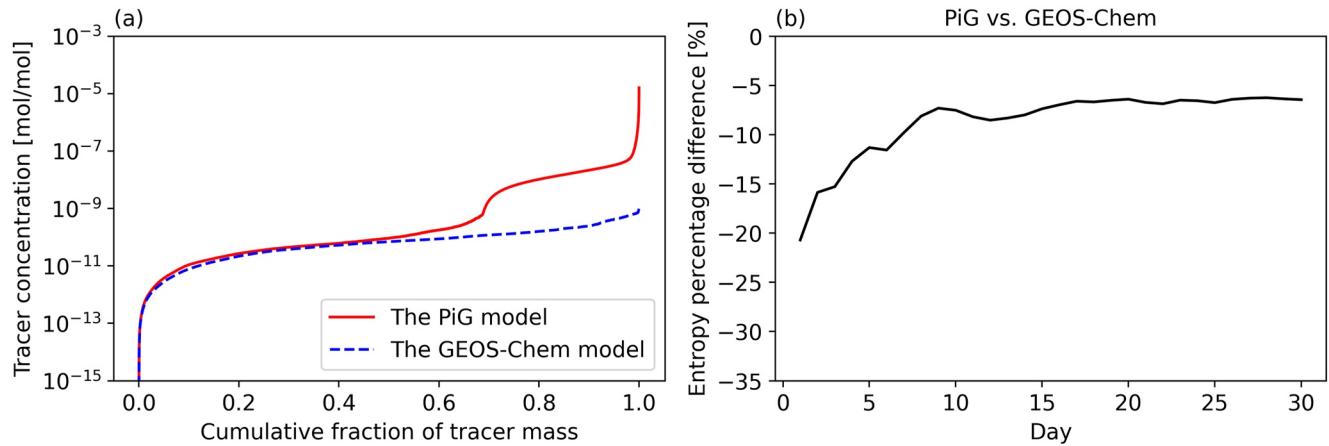


**Figure 10.** (a) The sorted tracer concentration (in ascending order) versus the cumulative tracer mass fraction at the end of the simulation. (b) The time series of the entropy percentage difference between the Plume-in-Grid (PiG) and global Eulerian (GEOS-Chem) model results (PiG minus GEOS-Chem model results).

According to previous studies (Lauritzen & Thuburn, 2012; Zhuang et al., 2018), entropy ( $S_\phi$ ) is adopted here to quantify the injected tracer diffusion:

$$S_\phi = -k_B \sum_{i=1}^N m_i \phi_i \log \phi_i \quad (14)$$

where  $k_B$  is the Boltzmann constant,  $N$  is the total number of grid cells of index  $i$ ,  $\phi_i$  is the tracer mixing ratio, and  $m_i$  is the air mass in the grid cell. Because continuous tracer injection (i.e., continuous plume segments injection) increases the entropy in both the PiG and GEOS-Chem model results, the entropy difference between the two model results (PiG vs. GEOS-Chem) reflects the difference in simulated tracer diffusion (larger entropy means more tracer diffusion). As shown in Figure 10b, the final entropy in the PiG model results is approximately 6% lower than that in the GEOS-Chem model results, which indicates that the PiG model can better preserve plumes to decrease tracer diffusion. For comparison, we also calculate the entropy which would be expected if the embedded plumes underwent no diffusion. Under this extreme case, the injected tracer would not be diffused, and the total entropy is conserved, which is 60% lower than the total entropy in the GEOS-Chem model results, compared to the 6% difference between the PiG and GEOS-Chem model results.

#### 4.2.3. Nonlinear Processes

Many chemical and aerosol processes (e.g., aerosol coagulation) are nonlinear processes that are highly dependent on concentration. Accurate estimation of nonlinear processes is essential in model simulations, which is especially true for the simulation of Accumulation-Mode (AM)  $\text{H}_2\text{SO}_4$  injection for solar geoengineering (Weisenstein et al., 2022). Second-order aerosol coagulation can greatly impact the particle size distribution of the injected AM  $\text{H}_2\text{SO}_4$ , which further influences the radiation transfer and climatic impacts of solar geoengineering in the simulation. Based on the hypothetical second-order process defined for the nonlinearity criterion in Section 2.5, we apply the same second-order process to the injected tracer in the PiG and GEOS-Chem models to compare the model performance in simulating the nonlinear process.

Under the same tracer injection scenario (Section 4.1), Figure 11 shows the total product mass of the second-order process and total CPU time in the PiG model (the horizontal resolution of the host GEOS-Chem model is  $2^\circ \times 2.5^\circ$ ) and the GEOS-Chem model at different horizontal resolutions ( $4^\circ \times 5^\circ$ ,  $2^\circ \times 2.5^\circ$ ,  $1^\circ \times 1.25^\circ$ , and  $0.5^\circ \times 0.625^\circ$ ). Compared to the GEOS-Chem

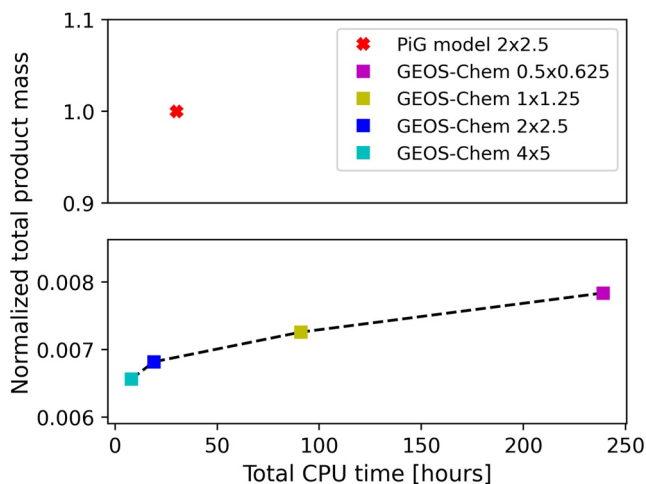


**Figure 11.** Sensitivity of chemical production from a hypothetical second-order process to computational effort for various model configurations. The total product of the process with a rate proportional to the square of injected tracer concentration is shown for various resolutions of global Eulerian-Chem compared to the Plume-in-Grid (PiG) model. The total product mass from different model results is normalized to that from the PiG model results.

model, the PiG model applies the Lagrangian plume model to resolve the subgrid plume segment, which results in a higher injected tracer concentration (Figure 10a). The higher injected tracer concentration ( $[C]$ ) results in a larger production rate ( $d[P]/dt$ ) in the PiG model than in the GEOS-Chem models, according to the hypothetical second-order process defined in Section 2.5 (i.e.,  $d[P]/dt = k[C]^2$ ). As a result, the final total product mass in the PiG model results (the red cross dot in Figure 11) is much larger than that in the GEOS-Chem model results (square dots in Figure 11). Figure 11 also shows that increasing the horizontal resolution of the GEOS-Chem model can increase the total product mass, which makes the total product mass closer to the PiG model results. However, a super-high horizontal resolution is required for the GEOS-Chem model to reach a similar total product mass as that in the PiG model results, which is implausible to achieve considering the computing efficiency. As we can see, even though the total product mass of the GEOS-Chem model at  $0.5^\circ \times 0.625^\circ$  (magenta square dot in Figure 11) is still much smaller than that of the PiG model (red cross dot in Figure 11), the CPU time required for the GEOS-Chem model simulation at  $0.5^\circ \times 0.625^\circ$  (239 CPU hr) is already much longer than that required for the PiG model simulation (30 CPU hr). Of course, the CPU time for the PiG model may change under different plume injection scenarios, as the computing resources for the PiG model are related to the number of plume segments simulated in the Lagrangian plume model. We also found that purely increasing the horizontal resolution of the GEOS-Chem model, without changing the vertical resolution, may cause additional vertical diffusion. Figure S3 in the Supporting Information S1 presents final vertical profiles of the global mean concentration in the GEOS-Chem model simulation at different horizontal resolutions ( $4^\circ \times 5^\circ$ ,  $2^\circ \times 2.5^\circ$ ,  $1^\circ \times 1.25^\circ$ , and  $0.5^\circ \times 0.625^\circ$ ). Purely increasing the horizontal resolution under a fixed vertical resolution may yield more vertical tracer dispersion of the injected tracer in the GEOS-Chem model (Text S4 in the Supporting Information S1). Thus, the vertical resolution needs to increase when the horizontal resolution increases to better preserve plumes in the stratosphere (Zhuang et al., 2018), which requires more computing resources.

## 5. Conclusions

A PiG model can be a computationally efficient way to improve the representation of subgrid-scale mixing, particularly in the case where mixing is driven by flow stretching that creates filamentary structures. We find evidence that the use of the PiG model could be a pathway to improving the numerical representation of nonlinear plume-scale processes in the stratosphere in a global Eulerian model. We compare the PiG model to a global Eulerian model (i.e., GEOS-Chem model) based on a 1-month simulation of continuous inert tracer emissions by aircraft in the stratosphere. Compared to the GEOS-Chem model, the PiG model has more high-concentration centers in the final total column concentration distribution (Figure 8a). The final total mass of injected tracer remaining in the injection area (60–40 hPa, 30°S to 30°N) in the PiG model is approximately 28% larger than that in the GEOS-Chem model (Figure 9a). Thus, the PiG model results show less plume dispersion than the GEOS-Chem model results. At the end of the simulation, approximately 1/3 of the injected tracer remains in the active plume segments in the PiG model, and is therefore at much higher tracer concentrations (2–4 orders of magnitude larger) than in the GEOS-Chem model. A metric, the entropy, is calculated based on the 3-D mixing ratio field of the injected tracer to quantify injected tracer mixing. The entropy from the PiG model results is approximately 6% lower than that from the GEOS-Chem model results, suggesting that the injected tracer experiences less mixing in the PiG model. With a hypothetical second-order process applied to the injected tracer, the final total product mass of the second-order process from the PiG model is approximately 2 orders of magnitude larger than that from the GEOS-Chem model (Figure 11). To reach the same total product mass as the PiG model, the GEOS-Chem model needs to greatly increase both the horizontal and vertical resolutions, which requires far more computing resources than does the PiG model. For example, the total product mass of the GEOS-Chem model at  $0.5^\circ \times 0.625^\circ$  (horizontal resolution) is still much smaller (2 orders of magnitude smaller) than that of the PiG model (with the host GEOS-Chem model at  $2^\circ \times 2.5^\circ$ ), but the CPU time required for the GEOS-Chem model simulation at  $0.5^\circ \times 0.625^\circ$  (239 CPU hr) is over seven times greater than that required for the PiG model simulation (30 CPU hr). Therefore, it is beneficial to embed a Lagrangian plume model into the global Eulerian model for subgrid plume simulations in the stratosphere. Otherwise, the global Eulerian model may underestimate both the tracer concentration and second-order processes of the subgrid plume.

This paper reports a first step in developing a PiG model that could be efficiently applied to a General Circulation Model (GCM) or a chemical transport model such as GEOS-Chem. The next step is to implement chemical and aerosol processes in the PiG model. There are opportunities to optimize the plume treatment by (a) adjusting the

resolution of the sub-models. A higher resolution of the plume model grid can better resolve the plume segment but requires more computing resources. For example, in the Lagrangian plume model, the 2-D grid is replaced by the 1-D grid in the mature plume phase based on a tradeoff between the computational efficiency (the 1-D grid model runs 90 times faster than the 2-D grid model) and accuracy (the percentage difference of center concentration between the 1-D and 2-D grid is within 10%, as shown in Figure 5); (b) considering plume overlapping. For the injected inert tracer in this study, the plume overlapping has a linear influence on the tracer concentration. Once the chemical and aerosol processes are involved in the PiG model, the tracer concentration would have a nonlinear change due to plume overlapping; (c) involving other regimes into the embedded plume model, such as the jet regime and vortex regime (Kärcher, 1995; Paoli & Shariff, 2016).

Our validation was limited to comparisons between the PiG model and GEOS-Chem models. Such validation can show that a PiG model reproduces a high-resolution Eulerian model, but in the long run, stratospheric plume models will need to be validated against observations. This might be accomplished using aircraft intercepts of plumes (Fahey et al., 1995), or balloon-based methods like that proposed for the Stratospheric Controlled Perturbation Experiment (SCoPEX) (Dykema et al., 2014), or hybrids of these methods. We hope that a multiscale PiG model, with the ability to resolve subgrid plumes in the stratosphere, will provide a more accurate simulation of applications in aircraft/rocket plume simulation, solar geoengineering, convective injections, stratospheric intrusions, intercontinental pollution, and small volcanic eruptions.

## Data Availability Statement

Data generated and investigated in this work are openly available on Harvard Dataverse (<https://doi.org/10.7910/DVN/KSFJ43>). The MERRA2 reanalysis data set is available from <https://gmao.gsfc.nasa.gov/reanalysis/MERRA-2/>. GEOS-Chem version 13.0.0 can be accessed from <https://doi.org/10.5281/zenodo.4618180>.

## Acknowledgments

This work was funded by Harvard's Solar Geoengineering Research Program. We would like to thank Debra Weisenstein, Akshat Agarwal, and Thibaud Fritz for discussing the plume model development. We thank the three anonymous reviewers for their constructive comments, which helped to greatly improve the analysis and presentation of this work. The computations in this study were run on the FASRC Cannon cluster at Harvard University.

## References

- Adams, P. J., & Seinfeld, J. H. (2002). Predicting global aerosol size distributions in general circulation models. *Journal of Geophysical Research: Atmospheres*, 107(D19), AAC-4-1–AAC-4-23. <https://doi.org/10.1029/2001jd001010>
- Bey, I., Jacob, D. J., Yantosca, R. M., Logan, J. A., Field, B. D., Fiore, A. M., et al. (2001). Global modeling of tropospheric chemistry with assimilated meteorology: Model description and evaluation. *Journal of Geophysical Research*, 106(D19), 23073–23095. <https://doi.org/10.1029/2001jd000807>
- Burkhardt, U., & Kärcher, B. (2009). Process-based simulation of contrail cirrus in a global climate model. *Journal of Geophysical Research*, 114(D16), D16201. <https://doi.org/10.1029/2008jd011491>
- Cameron, M. A., Jacobson, M. Z., Naiman, A. D., & Lele, S. K. (2013). Effects of plume-scale versus grid-scale treatment of aircraft exhaust photochemistry. *Geophysical Research Letters*, 40(21), 5815–5820. <https://doi.org/10.1002/2013gl057665>
- Cariolle, D., Caro, D., Paoli, R., Hauglustaine, D. A., Cuénot, B., Cozic, A., & Paugam, R. (2009). Parameterization of plume chemistry into large-scale atmospheric models: Application to aircraft NO<sub>x</sub> emissions. *Journal of Geophysical Research*, 114(D19), D19302. <https://doi.org/10.1029/2009jd011873>
- Dai, Z., Weisenstein, D. K., & Keith, D. W. (2018). Tailoring meridional and seasonal radiative forcing by sulfate aerosol solar geoengineering. *Geophysical Research Letters*, 45(2), 1030–1039. <https://doi.org/10.1002/2017gl076472>
- Dong, L., & Wang, B. (2012). Trajectory-tracking scheme in Lagrangian form for solving linear advection problems: Preliminary tests. *Monthly Weather Review*, 140(2), 650–663. <https://doi.org/10.1175/mwr-d-10-05026.1>
- Dürbeck, T., & Gerz, T. (1995). Large-eddy simulation of aircraft exhaust plumes in the free atmosphere: Effective diffusivities and cross-sections. *Geophysical Research Letters*, 22(23), 3203–3206. <https://doi.org/10.1029/95GL03021>
- Dürbeck, T., & Gerz, T. (1996). Dispersion of aircraft exhausts in the free atmosphere. *Journal of Geophysical Research*, 101(D20), 26007–26015. <https://doi.org/10.1029/96JD02217>
- Dykema, J. A., Keith, D. W., Anderson, J. G., & Weisenstein, D. (2014). Stratospheric controlled perturbation experiment: A small-scale experiment to improve understanding of the risks of solar geoengineering. *Philosophical Transactions of the Royal Society A: Mathematical, Physical & Engineering Sciences*, 372(2031), 20140059. <https://doi.org/10.1098/rsta.2014.0059>
- Eastham, S. D., & Jacob, D. J. (2017). Limits on the ability of global Eulerian models to resolve intercontinental transport of chemical plumes. *Atmospheric Chemistry and Physics*, 17(4), 2543–2553. <https://doi.org/10.5194/acp-17-2543-2017>
- Fahey, D. W., Keim, E. R., Boering, K. A., Brock, C. A., Wilson, J. C., Jonsson, H. H., et al. (1995). Emission measurements of the concorde supersonic aircraft in the lower stratosphere. *Science*, 270(5233), 70–74. <https://doi.org/10.1126/science.270.5233.70>
- Fritz, T. M., Eastham, S. D., Speth, R. L., & Barrett, S. R. H. (2020). The role of plume-scale processes in long-term impacts of aircraft emissions. *Atmospheric Chemistry and Physics*, 20(9), 5697–5727. <https://doi.org/10.5194/acp-20-5697-2020>
- Gelaro, R., McCarty, W., Suarez, M. J., Todling, R., Molod, A., Takacs, L., et al. (2017). The Modern-Era retrospective analysis for research and applications, version 2 (MERRA-2). *Journal of Climate*, 30(13), 5419–5454. <https://doi.org/10.1175/jcli-d-16-0758.1>
- Georgopoulos, P. G., & Seinfeld, J. H. (1986). Mathematical modeling of turbulent reacting plumes—I. General theory and model formulation. *Atmospheric Environment*, 20(9), 1791–1807. [https://doi.org/10.1016/0004-6981\(86\)90128-9](https://doi.org/10.1016/0004-6981(86)90128-9)
- Golja, C. M., Chew, L. W., Dykema, J. A., & Keith, D. W. (2021). Aerosol dynamics in the near field of the SCoPEX stratospheric balloon experiment. *Journal of Geophysical Research: Atmospheres*, 126(4), e2020JD033438. <https://doi.org/10.1029/2020jd033438>

- Jacobson, M. Z., Wilkerson, J. T., Naiman, A. D., & Lele, S. K. (2013). The effects of aircraft on climate and pollution. Part II: 20-year impacts of exhaust from all commercial aircraft worldwide treated individually at the subgrid scale. *Faraday Discussions*, 165, 369–382. <https://doi.org/10.1039/c3fd00034f>
- Karamchandani, P., Santos, L., Sykes, I., Zhang, Y., Tonne, C., & Seigneur, C. (2000). Development and evaluation of a state-of-the-science reactive plume model. *Environmental Science & Technology*, 34(5), 870–880. <https://doi.org/10.1021/es990611v>
- Karamchandani, P., Seigneur, C., Vijayaraghavan, K., & Wu, S.-Y. (2002). Development and application of a state-of-the-science plume-in-grid model. *Journal of Geophysical Research*, 107(D19). ACH-12-11–ACH-12-13. <https://doi.org/10.1029/2002jd002123>
- Karamchandani, P., Vijayaraghavan, K., Chen, S.-Y., Seigneur, C., & Edgerton, E. S. (2006). Plume-in-grid modeling for particulate matter. *Atmospheric Environment*, 40(38), 7280–7297. <https://doi.org/10.1016/j.atmosenv.2006.06.033>
- Kärcher, B. (1995). A trajectory box model for aircraft exhaust plumes. *Journal of Geophysical Research*, 100(D9), 18835–18844. <https://doi.org/10.1029/95JD01638>
- Konopka, P. (1995). Analytical Gaussian solutions for anisotropic diffusion in a linear shear flow. *Journal of Non-Equilibrium Thermodynamics*, 20(1), 78–91. <https://doi.org/10.1515/jnet.1995.20.1.78>
- Korsakissok, I., & Mallet, V. (2010). Development and application of a reactive plume-in-grid model: Evaluation over greater Paris. *Atmospheric Chemistry and Physics*, 10(18), 8917–8931. <https://doi.org/10.5194/acp-10-8917-2010>
- Kraabøl, A. G., Konopka, P., Stordal, F., & Schlager, H. (2000). Modelling chemistry in aircraft plumes I: Comparison with observations and evaluation of a layered approach. *Atmospheric Environment*, 34, 3939–3950. [https://doi.org/10.1016/S1352-2310\(00\)00156-4](https://doi.org/10.1016/S1352-2310(00)00156-4)
- Lauritzen, P. H., & Thuburn, J. (2012). Evaluating advection/transport schemes using interrelated tracers, scatter plots and numerical mixing diagnostics. *Quarterly Journal of the Royal Meteorological Society*, 138(665), 906–918. <https://doi.org/10.1002/qj.986>
- McKenna, D. S., Konopka, P., Grooß, J.-U., Günther, G., Müller, R., Spang, R., et al. (2002). A new Chemical Lagrangian Model of the Stratosphere (CLaMS) 1. Formulation of advection and mixing. *Journal of Geophysical Research*, 107(D16). ACH-15-11–ACH-15-15. <https://doi.org/10.1029/2000jd000114>
- Meijer, E. W., vanVelthoven, P. F. J., Wauben, W. M. F., Beck, J. P., & Velders, G. J. M. (1997). The effects of the conversion of nitrogen oxides in aircraft exhaust plumes in global models. *Geophysical Research Letters*, 24(23), 3013–3016. <https://doi.org/10.1029/97gl53156>
- Naiman, A. D., Lele, S. K., Wilkerson, J. T., & Jacobson, M. Z. (2010). Parameterization of subgrid plume dilution for use in large-scale atmospheric simulations. *Atmospheric Chemistry and Physics*, 10(5), 2551–2560. <https://doi.org/10.5194/acp-10-2551-2010>
- Newman, P. A., Wilson, J. C., Ross, M. N., Brock, C. A., Sheridan, P. J., Schoeberl, M. R., et al. (2001). Chance encounter with a stratospheric kerosene rocket plume from Russia over California. *Geophysical Research Letters*, 28(6), 959–962. <https://doi.org/10.1029/2000gl011972>
- Paoli, R. (2020). Modeling emissions from concentrated sources into large-scale models: Theory and apriori testing. *Atmosphere*, 11(8), 863. <https://doi.org/10.3390/atmos11080863>
- Paoli, R., Cariolle, D., & Sausen, R. (2011). Review of effective emissions modeling and computation. *Geoscientific Model Development*, 4(3), 643–667. <https://doi.org/10.5194/gmd-4-643-2011>
- Paoli, R., Poubeau, A., & Cariolle, D. (2020). Large-eddy simulations of a reactive solid rocket motor plume. *AIAA Journal*, 58(4), 1639–1656. <https://doi.org/10.2514/1.j058601>
- Paoli, R., & Shariff, K. (2016). Contrail modeling and simulation. *Annual Review of Fluid Mechanics*, 48(1), 393–427. <https://doi.org/10.1146/annurev-fluid-010814-013619>
- Pierce, J. R., Weisenstein, D. K., Heckendorn, P., Peter, T., & Keith, D. W. (2010). Efficient formation of stratospheric aerosol for climate engineering by emission of condensable vapor from aircraft. *Geophysical Research Letters*, 37(18), L18805. <https://doi.org/10.1029/2010gl043975>
- Rastigejev, Y., Park, R., Brenner, M. P., & Jacob, D. J. (2010). Resolving intercontinental pollution plumes in global models of atmospheric transport. *Journal of Geophysical Research*, 115(D2), D02302. <https://doi.org/10.1029/2009jd012568>
- Schumann, U. (2012). A contrail cirrus prediction model. *Geoscientific Model Development*, 5(3), 543–580. <https://doi.org/10.5194/gmd-5-543-2012>
- Schumann, U., Konopka, P., Baumann, R., Busen, R., Gerz, T., Schlager, H., et al. (1995). Estimate of diffusion parameters of aircraft exhaust plumes near the tropopause from nitric oxide and turbulence measurements. *Journal of Geophysical Research*, 100(D7), 14147–14162. <https://doi.org/10.1029/95jd01277>
- Tilmes, S., Richter, J. H., Mills, M. J., Kravitz, B., MacMartin, D. G., Garcia, R. R., et al. (2018). Effects of different stratospheric SO<sub>2</sub> injection altitudes on stratospheric chemistry and dynamics. *Journal of Geophysical Research: Atmospheres*, 123(9), 4654–4673. <https://doi.org/10.1002/2017jd028146>
- Vattioni, S., Weisenstein, D., Keith, D., Feinberg, A., Peter, T., & Stenke, A. (2019). Exploring accumulation-mode H<sub>2</sub>SO<sub>4</sub> versus SO<sub>2</sub> stratospheric sulfate geoengineering in a sectional aerosol–chemistry–climate model. *Atmospheric Chemistry and Physics*, 19(7), 4877–4897. <https://doi.org/10.5194/acp-19-4877-2019>
- Walcek, C. (2004). A Gaussian dispersion/plume model explicitly accounting for wind shear. *13th joint conference on the applications of air pollution meteorology with the air and waste management association*.
- Weisenstein, D. K., Vattioni, D., Franke, H., Niemeier, U., Vattioni, S., Chiodo, G., et al. (2022). A model intercomparison of stratospheric solar geoengineering by accumulation-mode sulfate aerosols. *Atmospheric Chemistry and Physics*, 22, 2955–2973. <https://doi.org/10.5194/acp-22-2955-2022>
- Zhuang, J., Jacob, D. J., & Eastham, S. D. (2018). The importance of vertical resolution in the free troposphere for modeling intercontinental plumes. *Atmospheric Chemistry and Physics*, 18(8), 6039–6055. <https://doi.org/10.5194/acp-18-6039-2018>